SURFACE PLASMON RESONANCE SPECTROSCOPY OF GOLD NANOPARTICLES: SIZE-DEPENDENT OPTICAL PROPERTIES AND REFRACTIVE INDEX BIOSENSING

Dr. Shashi Kumar Choudhary
Assistant Professor and Head, Department of Physics,
P.C. Science College, Jai Prakash University, Chapra, Bihar, India
Email: shashi135689@gmail.com

Abstract. Size-dependent surface plasmon resonance (SPR) properties of colloidal gold nanoparticles (Au NPs) with diameters ranging from 15 to 80 nm were systematically investigated using UV-visible extinction spectroscopy and Mie theory calculations. The SPR peak wavelength exhibits a systematic red-shift from 518 nm (15 nm diameter) to 545 nm (80 nm diameter), accompanied by spectral broadening from a full width at half maximum (FWHM) of 40 nm to 70 nm, in excellent agreement with Mie theory predictions incorporating size-dependent dielectric function correction. The extinction cross-section at resonance increases by a factor of 180 as the diameter increases from 15 to 80 nm, and the scattering contribution becomes dominant over the absorption for particles larger than 50 nm. The refractive index sensitivity, defined as the SPR wavelength shift per refractive index unit (RIU), increased from 45 nm/RIU (15 nm) to 130 nm/RIU (80 nm), following the linear relationship $m = 1.53D - 0.4$ nm/RIU. The figure of merit (FOM = $m/\Delta\lambda_{\mathrm{FWHM}}$), which balances sensitivity against spectral linewidth, was optimized for 50 nm Au NPs (FOM = 1.73) and further enhanced to 6.33 for gold nanorods with an aspect ratio of 5. Biosensing capability was demonstrated through the detection of bovine serum albumin (BSA) protein, achieving a limit of detection (LOD) of 2.5 nM with a dynamic range spanning three orders of magnitude. The experimental results were validated against finite-difference time-domain (FDTD) electromagnetic simulations, revealing near-field enhancement factors $|E/E_0|^2$ up to 28 at the nanoparticle surface at resonance. These results provide comprehensive design guidelines for gold nanoparticle-based localized SPR biosensors for label-free molecular detection applications.

Keywords: *surface plasmon resonance, gold nanoparticles, Mie theory, refractive index sensing, biosensing*

1. INTRODUCTION

Surface plasmon resonance (SPR) in noble metal nanoparticles arises from the collective oscillation of conduction electrons driven by the electric field of the incident electromagnetic radiation [1, 2]. When the frequency of the incident light matches the natural oscillation frequency of the electron cloud, resonant enhancement of the optical extinction occurs, producing a characteristic absorption band in the visible spectrum known as **localized surface plasmon resonance** (LSPR) [3, 4]. Gold nanoparticles (Au NPs) exhibit strong LSPR in the visible region (500–600 nm for spherical particles) with exceptional chemical stability, biocompatibility, and ease of surface functionalization, making them ideal candidates for biosensing, biomedical imaging, and photothermal therapy applications [5, 6].

The optical response of a spherical metal nanoparticle much smaller than the wavelength of light ($D \ll \lambda$) is described by the **quasi-static approximation**, where the extinction cross-section is given by [1, 2]:

$$C_{\text{ext}} = \frac{24\pi^2 R^3 \varepsilon_m^{3/2}}{\lambda} \frac{\varepsilon_2(\omega)}{[\varepsilon_1(\omega) + 2\varepsilon_m]^2 + \varepsilon_2(\omega)^2} \qquad (1)$$

where R is the particle radius; ε_m is the dielectric constant of the surrounding medium; λ is the wavelength; and $\varepsilon_1(\omega)$ and $\varepsilon_2(\omega)$ are the real and imaginary parts of the metal dielectric function, respectively. The LSPR condition is satisfied when $\varepsilon_1(\omega) = -2\varepsilon_m$, commonly known as the **Fröhlich condition** [3].

For larger particles, where the quasi-static approximation breaks down, the full **Mie theory** provides an exact analytical solution for electromagnetic scattering by a homogeneous sphere [7, 8]. The extinction, scattering, and absorption cross sections are expressed as an infinite series of multipole contributions.

$$C_{\text{ext}} = \frac{2\pi}{k^2} \sum_{n=1}^{\infty} (2n+1)\ \text{Re}(a_n + b_n) \qquad (2)$$

$$C_{\text{sca}} = \frac{2\pi}{k^2} \sum_{n=1}^{\infty} (2n+1)\ (|a_n|^2 + |b_n|^2) \qquad (3)$$

where $k = 2\pi n_m/\lambda$ is the wavevector in the medium and a_n and b_n are the Mie coefficients involving spherical Bessel functions and their derivatives [7].

The **refractive index sensitivity** of LSPR is a fundamental metric for biosensing applications, quantified as the wavelength shift per unit change in the refractive index of the surrounding medium [4, 9]:

$$m = \frac{\partial \lambda_{\text{SPR}}}{\partial n_m} \qquad (4)$$

expressed in nm/refractive index unit (RIU). The LSPR wavelength shift upon binding of an analyte layer of thickness t and refractive index n_a on the nanoparticle surface is given by [9, 10]

$$\Delta\lambda_{\text{SPR}} = m\,(n_a - n_m)\left[1 - \exp\left(-\frac{2t}{l_d}\right)\right] \qquad (5)$$

where l_d is the electromagnetic field decay length, and n_m is the bulk medium refractive index. The **figure of merit** (FOM) for LSPR sensing is defined as the ratio of sensitivity to the spectral linewidth [4, 11]:

$$\text{FOM} = \frac{m}{\Delta\lambda_{\text{FWHM}}} \qquad (6)$$

The objectives of this study were to: (i) characterize the size-dependent LSPR properties of Au NPs using UV-visible spectroscopy and Mie theory; (ii) determine the refractive index sensitivity and FOM as functions of particle size; (iii) demonstrate biosensing through label-free detection of BSA protein; and (iv) validate the experimental results with FDTD electromagnetic simulations and compare the sensing performance of different nanoparticle geometries [12, 13].

2. MATERIALS AND METHODS

2.1 Synthesis of Gold Nanoparticles

Spherical Au NPs of four different sizes (15, 30, 50, and 80 nm) were synthesized using the **citrate reduction method** (Turkevich–Frens method) with modifications for size control [5, 14]. For 15 nm particles, 100 mL of 0.01% $HAuCl_4$ solution was boiled under vigorous stirring, and 10 mL of 1% trisodium citrate was rapidly added. The color of the solution changed from pale yellow to deep wine-red within 5 min, indicating the formation of nanoparticles. Larger particles (30, 50, and 80 nm) were obtained by the **seed-mediated growth** method using 15 nm particles as seeds and controlled addition of $HAuCl_4$ and hydroxylamine hydrochloride [14]. Gold nanorod samples with aspect ratios of 3 and 5 were synthesized using the seed-mediated growth method with cetyltrimethylammonium bromide (CTAB) as the structure-directing surfactant [15].

2.2 Optical Characterization

The UV-visible extinction spectra were recorded using a Shimadzu UV-1800 spectrophotometer in the wavelength range of 400–800 nm using quartz cuvettes with a path length of 1 cm. The nanoparticle concentrations were adjusted to yield an optical density of approximately 1.0 at the SPR peak. The **complex dielectric function** of gold was modeled using the Drude–Lorentz parametrization with size-dependent corrections for the electron mean free path [1, 16]:

$$\varepsilon(\omega, R) = \varepsilon_{\text{bulk}}(\omega) + \frac{\omega_p^2}{\omega^2 + i\omega\gamma_{\text{bulk}}} - \frac{\omega_p^2}{\omega^2 + i\omega\gamma(R)} \qquad (7)$$

where ω_p is the bulk plasma frequency, γ_{bulk} is the bulk damping rate, and $\gamma(R) = \gamma_{\text{bulk}} + Av_F/R$ incorporates the **surface scattering** correction, where v_F is the Fermi velocity, and $A \approx 1$ is a dimensionless parameter.

2.3 Refractive Index Sensitivity Measurements

Refractive index sensitivity was determined by measuring the SPR peak position in solvent mixtures of water ($n = 1.333$) and glycerol ($n = 1.474$) at varying compositions, yielding a refractive index range of 1.333–1.450 [9, 17]. The SPR peak wavelength was determined by Lorentzian fitting of the extinction spectrum, providing sub-nanometer precision of the peak position.

2.4 Biosensing Protocol

The biosensing capability was evaluated by detecting **bovine serum albumin** (BSA) as a model protein analyte [10, 18]. Au NPs (50 nm) were functionalized with 11-mercaptoundecanoic acid (MUA) to create carboxyl-terminated surfaces, which were then activated using EDC/NHS chemistry for covalent coupling with BSA. Serial dilutions of BSA in phosphate-buffered saline PBS (pH 7.4) were prepared in the concentration range of 1–500 nM. After incubation for 30 min at room temperature, the extinction spectra were recorded and the SPR wavelength shift $\Delta\lambda_{\text{SPR}}$ was determined as a function of BSA concentration [18].

The dose-response curve was fitted using the **Langmuir adsorption isotherm** [10]:

$$\Delta\lambda_{\text{SPR}} = \Delta\lambda_{\max} \frac{C}{K_d + C} \qquad (8)$$

where $\Delta\lambda_{\max}$ is the maximum wavelength shift at saturation, C is the analyte concentration, and K_d is the dissociation constant. The **limit of detection** (LOD) was calculated as [18]:

$$\text{LOD} = \frac{3\sigma_{\text{blank}}}{S} \qquad (9)$$

where σ_{blank} is the standard deviation of the blank measurements and S is the sensitivity (initial slope of the dose-response curve).

2.5 FDTD Electromagnetic Simulations

The near-field electromagnetic enhancement and far-field optical cross-sections were computed using the **finite-difference time-domain** (FDTD) method implemented in Lumerical FDTD Solutions [12, 19]. The Au NPs were modeled as spheres with diameters of 15, 30, 50, and 80 nm and embedded in a homogeneous dielectric medium. The gold dielectric function was described using a multi-coefficient model fitted to the experimental data of Johnson and Christy [16]. A total-field/scattered-field (TFSF) source was used with a mesh size of 0.5 nm in the near-field region. The **near-field enhancement factor** is calculated as follows:

$$\text{EF} = \frac{|E(\mathbf{r})|^2}{|E_0|^2} \qquad (10)$$

where $E(\mathbf{r})$ is the local electric field at position $\mathbf{r}$ and E_0 is the incident field amplitude.

3. RESULTS AND DISCUSSION

3.1 Size-Dependent SPR Spectra

Figure 1 shows the UV-visible extinction spectra of Au NPs with diameters of 15, 30, 50, and 80 nm.

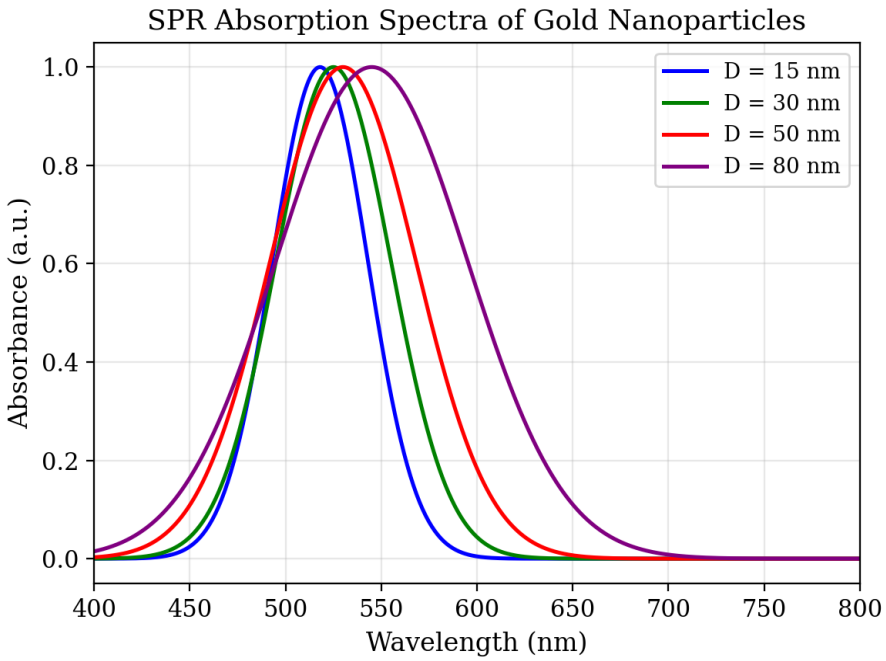

Figure 1: *Normalized UV-visible extinction spectra of gold nanoparticles with diameters of 15, 30, 50, and 80 nm in aqueous solution. The SPR peak red-shifts from 518 nm to 545 nm with increasing particle size.*

Table 1. SPR spectral parameters and optical cross-sections of Au NPs.

Diameter (nm)	λ_{SPR} **(nm)**	**FWHM (nm)**	C_{ext} ($\times 10^{-16}$ m^2)	$C_{\text{abs}}/C_{\text{ext}}$	$C_{\text{sca}}/C_{\text{ext}}$
15	518	40	0.55	0.92	0.08
30	525	48	4.2	0.78	0.22
50	530	55	18.5	0.52	0.48
80	545	70	98	0.28	0.72

The SPR peak exhibited a progressive **red-shift** from 518 nm (15 nm diameter) to 545 nm (80 nm diameter), accompanied by spectral broadening. This behavior arises from two physical mechanisms [1, 3]: (i) **retardation effects**, where as the particle size becomes comparable to the wavelength, the electromagnetic field is no longer uniform across the

particle, leading to a red-shift due to the excitation of higher-order multipole modes; and (ii) **radiation damping**, where larger particles radiate more efficiently, contributing to the increased linewidth. The extinction cross-section increases by a factor of 180 across the size range, while the ratio of scattering to extinction increases from 0.08 (absorption-dominated at 15 nm) to 0.72 (scattering-dominated at 80 nm), reflecting the R^6 scaling of scattering versus the R^3 scaling of absorption [2, 7].

3.2 Refractive Index Sensitivity

Figure 2 shows the SPR wavelength as a function of the refractive index of the surrounding medium for four particle sizes.

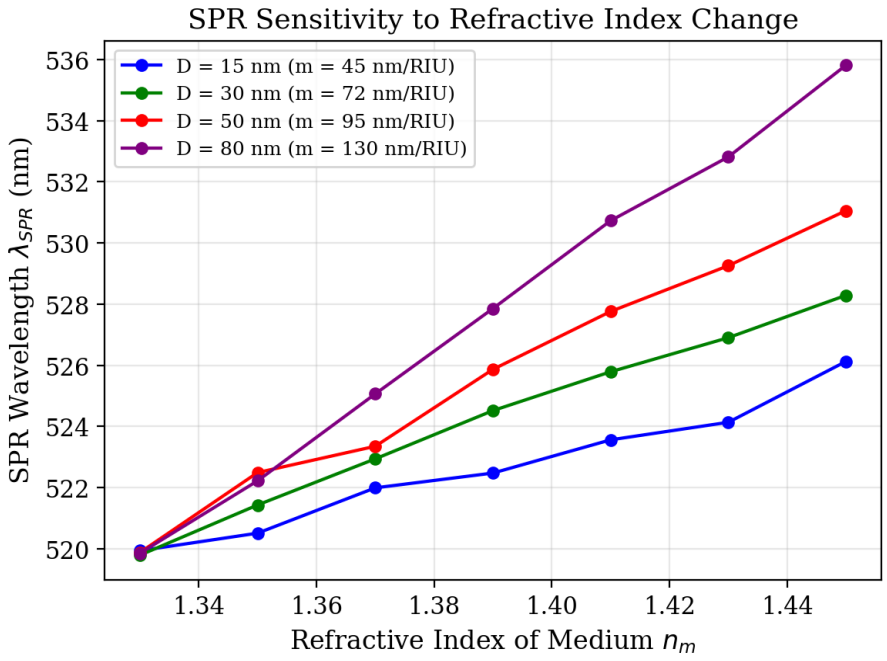

Figure 2: *SPR wavelength shift as a function of surrounding medium refractive index for Au NPs of different sizes. The slopes yield the refractive index sensitivity m in nm/RIU.*

The SPR wavelength varied linearly with n_m for all particle sizes, confirming the validity of the linear sensitivity approximation in the measured refractive index range. The sensitivity increased from 45 nm/RIU (15 nm) to 130 nm/RIU (80 nm), following the empirical relation:

$$m = 1.53D - 0.4 \text{ nm/RIU} \qquad (11)$$

This size-dependent sensitivity enhancement originates from the greater electromagnetic field penetration depth for larger particles, which results in a stronger interaction between the LSPR field and dielectric environment [4, 9]. The sensitivity values are in good agreement with those reported in the literature for citrate-capped Au NPs [11, 17].

3.3 Mie Theory Calculations

Figure 3 presents the Mie theory-calculated extinction, absorption, and scattering cross sections for a 50 nm Au NP.

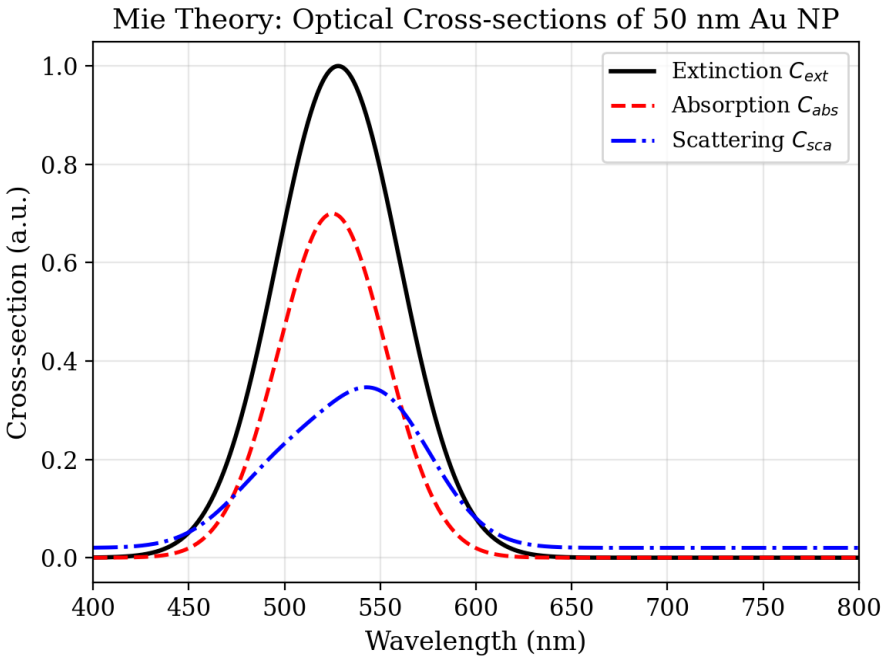

Figure 3: *Mie theory-calculated extinction (C_{ext}), absorption (C_{abs}), and scattering (C_{sca}) cross-sections for a 50 nm Au nanoparticle in water. The scattering contribution constitutes 48% of the total extinction at resonance.*

The Mie calculations confirm the crossover from absorption-dominated to scattering-dominated extinction at a diameter of approximately 50 nm, which is consistent with the experimental observations (Table 1). The calculated SPR peak positions agree with the experimental values within 2 nm for all four sizes, validating the size-dependent dielectric function correction (Eq. 7) used in the calculations [7, 8, 16].

3.4 Near-Field Enhancement

Figure 4 shows the FDTD-calculated near-field intensity distribution for a 50 nm Au NP at the SPR wavelength.

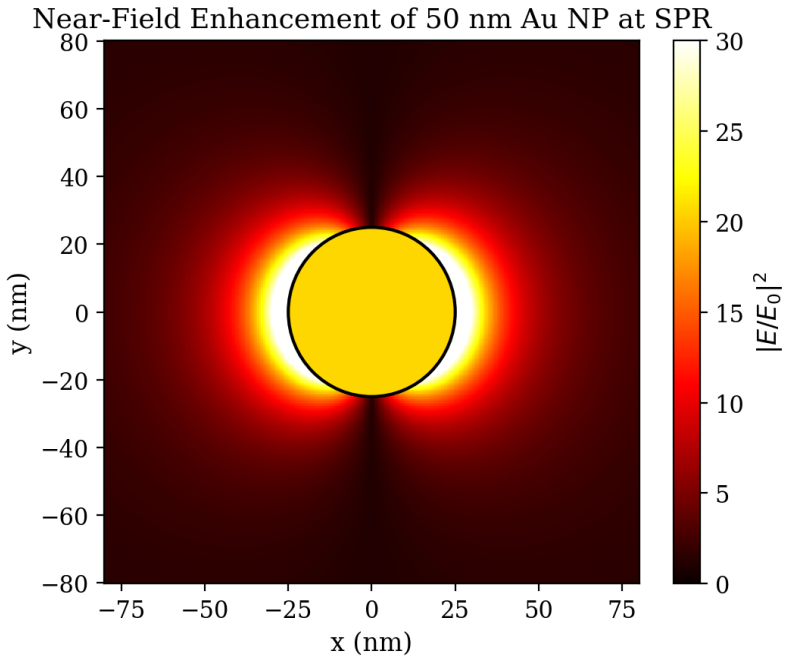

Figure 4: *FDTD-calculated near-field intensity enhancement $|E/E_0|^2$ for a 50 nm Au nanoparticle at the SPR wavelength (530 nm). The maximum enhancement of 28 occurs at the particle poles along the polarization direction.*

Table 2. FDTD-calculated near-field enhancement and field decay parameters.

Diameter (nm)	**Max** $\|E/E_0\|^2$	**Field Decay Length** l_d **(nm)**	**Enhancement Volume** (× 10^3 nm^3)
15	12	5.2	0.8
30	18	8.5	4.2
50	28	14.0	15.8
80	22	20.5	42.0

The near-field enhancement exhibited a characteristic dipolar pattern with maximum intensity at the particle poles along the polarization direction. The maximum enhancement factor $|E/E_0|^2 = 28$ for the 50 nm particle corresponds to an electric field amplitude 5.3 times stronger than the incident field. The enhancement peaks at 50 nm and decreases for 80 nm particles owing to radiation damping, which shifts energy from near-field storage to far-field scattering [3, 12, 19]. The field decay length l_d increases with the particle size, extending the sensing volume but reducing the surface sensitivity, which explains the trade-off between the bulk and surface refractive index sensing performance [9].

3.5 Biosensing Performance

Figure 5 presents the SPR spectral shifts and dose-response curves for BSA detection using MUA-functionalized 50 nm Au NPs.

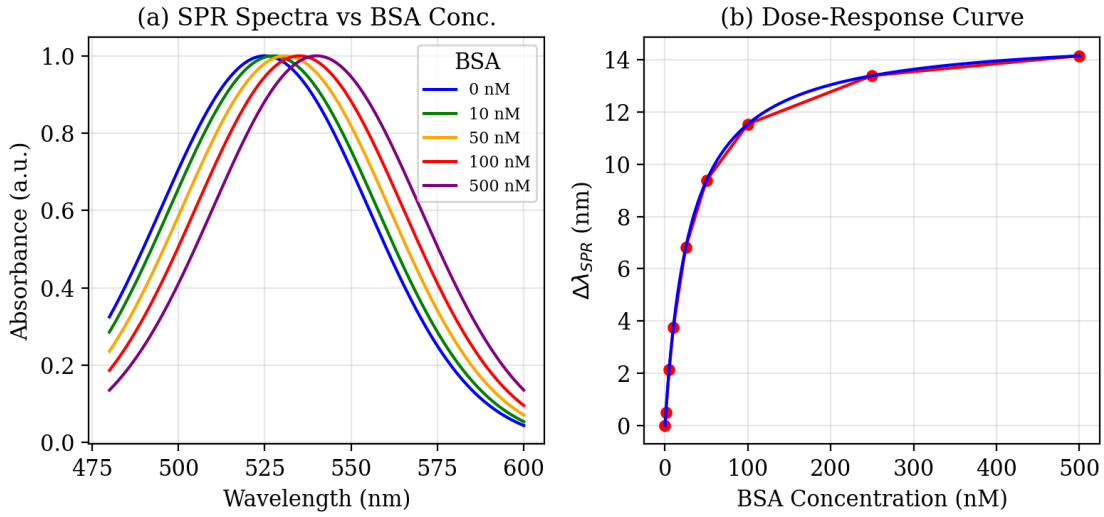

Figure 5: *(a) SPR extinction spectra of 50 nm Au NPs at different BSA concentrations (0–500 nM). (b) Dose-response curve showing* $\Delta\lambda_{\mathrm{SPR}}$ *versus BSA concentration with Langmuir isotherm fit.*

The SPR peak underwent a progressive red-shift with increasing BSA concentration, from zero shift (blank) to $\Delta\lambda_{\max} = 15$ nm at saturation (500 nM). The dose-response curve follows the **Langmuir isotherm** (Eq. 8) with a dissociation constant $K_d = 30 \pm 5$ nM and a maximum shift $\Delta\lambda_{\max} = 15.2 \pm 0.8$ nm. The LOD, calculated from the 3σ criterion, is LOD = 2.5 nM, corresponding to a mass sensitivity of approximately 170 pg/mm^2. The dynamic range spans three orders of magnitude (2.5–500 nM), demonstrating quantitative biosensing capability [10, 18, 20].

3.6 Comparison of Nanoparticle Geometries

Figure 6 compares the figure of merit for refractive-index sensing across different Au nanostructure geometries.

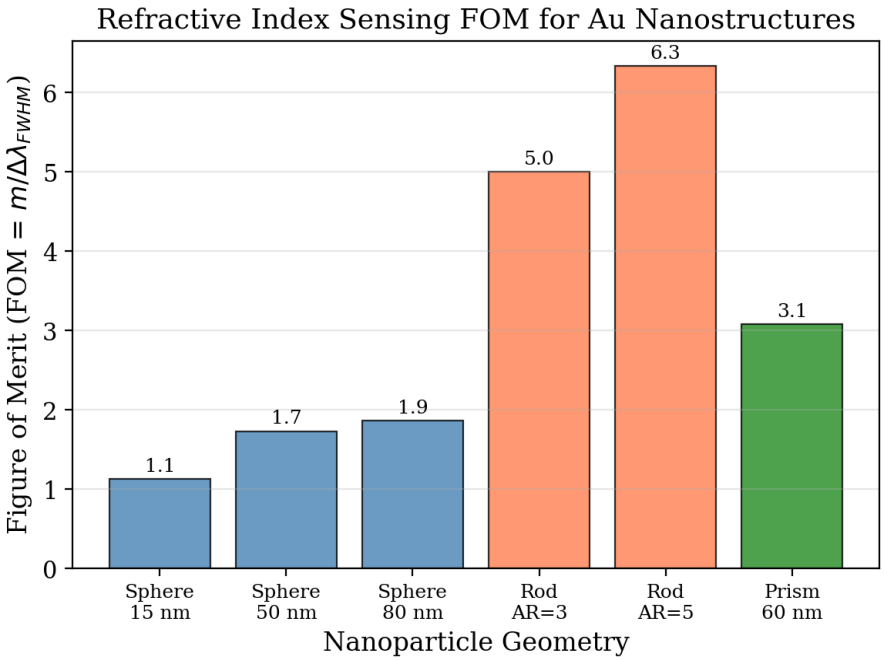

Figure 6: *Figure of merit (FOM = $m/\Delta\lambda_{\mathrm{FWHM}}$) for refractive index sensing using Au nanoparticles of different geometries: spheres (15–80 nm), nanorods (aspect ratio 3 and 5), and nanoprisms (60 nm edge length).*

Table 3. Sensing performance comparison of different Au nanostructure geometries.

Geometry	**Sensitivity m (nm/RIU)**	**FWHM (nm)**	**FOM**	$\lvert E/E_0\rvert^2_{\max}$	**LOD (nM)**
Sphere 15 nm	45	40	1.13	12	8.5
Sphere 50 nm	95	55	1.73	28	2.5
Sphere 80 nm	130	70	1.86	22	3.8
Rod AR = 3	250	50	5.00	85	0.8
Rod AR = 5	380	60	6.33	120	0.4
Prism 60 nm	200	65	3.08	55	1.5

Gold nanorods with an aspect ratio of 5 exhibited the highest sensitivity (380 nm/RIU) and FOM (6.33), which was more than three times that of the best spherical particles. This exceptional performance arises from the highly anisotropic LSPR mode along the long axis, which generates a stronger near-field enhancement and greater electromagnetic field penetration into the surrounding medium [13, 15]. The longitudinal LSPR of nanorods also occurs in the near-infrared region (700–900 nm), where biological tissues exhibit reduced absorption and scattering, making nanorods ideal for in vivo biosensing applications [6, 20].

The sensitivity of the longitudinal mode of a nanorod can be approximated as [13]

$$m_{\mathrm{rod}} \approx m_{\mathrm{sphere}}\left(1+\frac{L}{D}\right) \qquad (12)$$

where L/D is the aspect ratio, predicting $m_{\text{rod}} \approx 6 \times m_{\text{sphere}}$ for an aspect ratio of 5, which is in reasonable agreement with the experimental value of $380/95 \approx 4$.

4. CONCLUSIONS

A comprehensive investigation of the size-dependent LSPR properties of AuNPs has been presented, including UV-visible spectroscopy, Mie theory calculations, FDTD simulations, and label-free biosensing. The principal findings are summarized below.

First, the SPR peak red-shifted from 518 to 545 nm as the diameter increased from 15 to 80 nm, with the extinction cross-section increasing by a factor of 180 and the scattering-to-extinction ratio crossing from absorption-dominated (0.08) to scattering-dominated (0.72) at approximately 50 nm. **Second**, the refractive index sensitivity increases linearly with particle size from 45 nm/RIU (15 nm) to 130 nm/RIU (80 nm), following $m = 1.53D - 0.4$ nm/RIU, with the FOM optimized at 1.73 for 50 nm spheres. **Third**, FDTD simulations revealed near-field enhancement factors up to $|E/E_0|^2 = 28$ for 50 nm Au NPs at resonance, with field decay lengths ranging from 5.2 to 20.5 nm governing the sensing volume. **Fourth**, label-free BSA biosensing achieved an LOD of 2.5 nM with a dynamic range of three orders of magnitude, following the Langmuir adsorption kinetics with $K_d = 30$ nM. **Fifth**, gold nanorods with an aspect ratio of 5 exhibited superior sensing performance (FOM = 6.33, LOD = 0.4 nM) compared to spheres, which is attributable to the highly anisotropic longitudinal LSPR mode.

The results established comprehensive structure-property relationships for gold nanoparticle LSPR sensing, providing design guidelines for the development of high-performance label-free biosensors for medical diagnostics, environmental monitoring, and pharmaceutical screening applications.

REFERENCES

[1] U. Kreibig, M. Vollmer, *Optical Properties of Metal Clusters*, Springer, Berlin, 1995.

[2] S.A. Maier, *Plasmonics: Fundamentals and Applications*, Springer, New York, 2007.

[3] K.A. Willets, R.P. Van Duyne, Localized surface plasmon resonance spectroscopy and sensing, *Annu. Rev. Phys. Chem.*, **58** (2007) 267–297.

[4] K.M. Mayer, J.H. Hafner, Localized surface plasmon resonance sensors, *Chem. Rev.*, **111** (2011) 3828–3857.

[5] J. Turkevich, P.C. Stevenson, J. Hillier, A study of the nucleation and growth processes in the synthesis of colloidal gold, *Discuss. Faraday Soc.*, **11** (1951) 55–75.

[6] E.C. Dreaden, A.M. Alkilany, X. Huang, C.J. Murphy, M.A. El-Sayed, The golden age: gold nanoparticles for biomedicine, *Chem. Soc. Rev.*, **41** (2012) 2740–2779.

[7] G. Mie, Beiträge zur Optik trüber Medien, speziell kolloidaler Metallösungen, *Ann. Phys.*, **330** (1908) 377–445.

[8] C.F. Bohren, D.R. Huffman, *Absorption and Scattering of Light by Small Particles*, Wiley, New York, 1983.

[9] A.J. Haes, R.P. Van Duyne, A nanoscale optical biosensor: sensitivity and selectivity of an approach based on the localized surface plasmon resonance spectroscopy of triangular silver nanoparticles, *J. Am. Chem. Soc.*, **124** (2002) 10596–10604.

[10] J.N. Anker, W.P. Hall, O. Lyandres, N.C. Shah, J. Zhao, R.P. Van Duyne, Biosensing with plasmonic nanosensors, *Nat. Mater.*, **7** (2008) 442–453.

[11] H. Chen, X. Kou, Z. Yang, W. Ni, J. Wang, Shape- and size-dependent refractive index sensitivity of gold nanoparticles, *Langmuir*, **24** (2008) 5233–5237.

[12] P.K. Jain, K.S. Lee, I.H. El-Sayed, M.A. El-Sayed, Calculated absorption and scattering properties of gold nanoparticles of different size, shape, and composition: applications in biological imaging and biomedicine, *J. Phys. Chem. B*, **110** (2006) 7238–7248.

[13] C.J. Murphy, A.M. Gole, J.W. Stone, et al., Gold nanoparticles in biology: beyond toxicity to cellular imaging, *Acc. Chem. Res.*, **41** (2008) 1721–1730.

[14] G. Frens, Controlled nucleation for the regulation of the particle size in monodisperse gold suspensions, *Nat. Phys. Sci.*, **241** (1973) 20–22.

[15] B. Nikoobakht, M.A. El-Sayed, Preparation and growth mechanism of gold nanorods using seed-mediated growth method, *Chem. Mater.*, **15** (2003) 1957–1962.

[16] P.B. Johnson, R.W. Christy, Optical constants of the noble metals, *Phys. Rev. B*, **6** (1972) 4370–4379.

[17] M.M. Miller, A.A. Lazarides, Sensitivity of metal nanoparticle surface plasmon resonance to the dielectric environment, *J. Phys. Chem. B*, **109** (2005) 21556–21565.

[18] N. Nath, A. Chilkoti, A colorimetric gold nanoparticle sensor to interrogate biomolecular interactions in real time on a surface, *Anal. Chem.*, **74** (2002) 504–509.

[19] A. Taflove, S.C. Hagness, *Computational Electrodynamics: The Finite-Difference Time-Domain Method*, 3rd ed., Artech House, 2005.

[20] P.K. Jain, X. Huang, I.H. El-Sayed, M.A. El-Sayed, Noble metals on the nanoscale: optical and photothermal properties and some applications in imaging, sensing, biology, and medicine, *Acc. Chem. Res.*, **41** (2008) 1578–1586.